Raman scattering efficiency in $LiTaO_3$ and $LiNbO_3$ crystals

S. Sanna,* S. Neufeld, M. Rüsing, G. Berth, A. Zrenner, and W. G. Schmidt
Department Physik, Universität Paderborn, 33095 Paderborn, Germany
(Received 12 April 2015; revised manuscript received 19 May 2015; published 5 June 2015)

$LiTaO_3$ and $LiNbO_3$ crystals are investigated here in a combined experimental and theoretical study that uses Raman spectroscopy in a complete set of scattering geometries and corresponding density-functional theory calculations to provide microscopic information on their vibrational properties. The Raman scattering efficiency is computed from first principles in order to univocally assign the measured Raman peaks to the calculated eigenvectors. Measured and calculated Raman spectra are shown to be in qualitative agreement and confirm the mode assignment by Margueron *et al.* [J. Appl. Phys. **111**, 104105 (2012)], thus finally settling a long debate. While the two crystals show rather similar vibrational properties overall, the E-TO_9 mode is markedly different in the two oxides. The deviations are explained by a different anion-cation bond type in $LiTaO_3$ and $LiNbO_3$ crystals.

DOI: 10.1103/PhysRevB.91.224302 PACS number(s): 77.84.−s, 63.20.dk, 78.30.−j

I. INTRODUCTION

$LiTaO_3$ and $LiNbO_3$ are related ferroelectric oxides. At room temperature, they both crystallize in a ferroelectric structure belonging to the space group $R3c$ [1]. Starting from the 1970s up to now, both materials have been widely employed for the fabrication of electro-optic [2,3] and acousto-optic devices [4]. Accordingly, the two oxides have been intensively investigated by several experimental techniques [5,6]. Raman spectroscopy is one of the foremost tools for the analysis of the vibrational properties of molecules and solid-state systems [7]. It is commonly employed to characterize samples, as it leads to information about crystallinity, stoichiometry [8], strain [9], doping [10,11], etc. In particular, in combination with theoretical approaches yielding phonon eigenvectors such as the density functional theory (DFT), it is possible to assign a displacement pattern to each Raman peak and attain structural information from the peak modifications with temperature and composition. Thus, Raman spectroscopy has been used to investigate phase transitions [12,13], visualize ferroelectric domains [14–16], and even to establish the surface polarity [17].

Yet, the assignment of the phonon modes in $LiTaO_3$ and $LiNbO_3$ remained under discussion for a long time, as intrinsic and extrinsic defects, as well as the presence of modes with similar frequency or low Raman intensity, complicated the investigations [18]. Existing first-principles calculations did not clarify these controversies, as the assignment of the peaks was based only on the mode energy [19,20]. This procedure is not always reliable. In large systems with many vibrational modes, the mode assignment is not unambiguous, as many calculated phonons might have frequencies compatible with a given Raman peak. Furthermore, some of the calculated modes might have vanishing Raman intensity, which complicates the identification of the phonons. On the other side, modes which are not expected to be Raman active might appear in the recorded spectra, if a perturbation softens the selection rules (e.g., the presence of domain boundaries).

In this respect, the *ab initio* calculation of the Raman intensities [21–24] might be useful. Hermet *et al.*, e.g., have calculated for selected scattering configurations the nonresonant Raman scattering spectra of the ferroelectric phase of lithium niobate from first principles, with an implementation based on the nonlinear response formalism and taking advantage of the $2n + 1$ theorem [25]. This allowed for a different assignment of the E modes. Later, Margueron *et al.* presented a complete assignment of the E modes in $LiTaO_3$ and $LiNbO_3$ by comparing Raman and infrared data [26].

In this work we combine μ-Raman measurements and DFT calculations to identify the controversial phonon modes. We systematically measure and calculate the Raman spectra of $LiTaO_3$ and $LiNbO_3$ for all possible polarization configurations of incoming and scattered photons. The calculation of the Raman intensities allows for the conclusive assignment of the measured Raman peaks to the calculated phonon eigenvectors. The Raman intensities are calculated with an approach similar to the calculations of Ref. [25]. However, instead of using the density functional perturbation theory, the calculations are performed based on ground-state DFT calculations for frozen phonons [27].

Our results confirm the assignment proposed in Refs. [25,26], and thus resolve the long-standing debate concerning in particular the assignment of the E modes. The E TO_9 phonon mode, whose oscillator strength strongly differs in $LiTaO_3$ and $LiNbO_3$, is examined in some detail. The theoretical modeling of the scattering efficiencies is crucial for the assignment of phonon modes in complex systems, with a large number of modes or where selection rules are relaxed by the system morphology.

The paper is structured as follows: Sec. II describes the theoretical foundations of the Raman susceptibility calculations and computational details. The sample preparation and characterization together with the experimental details are given in Sec. III. In Sec. IV the results of this combined investigation are exposed and discussed. Finally, the main results of this work are summarized in Sec. V.

II. THEORY

A. Raman susceptibility

The Raman scattering efficiencies of zone center optical phonons can be calculated from first principles. The main

*simone.sanna@uni-paderborn.de

equations derived in Refs. [21–24] are briefly summarized in the following. Thereby, nonresonant Raman scattering is considered, in which the polarization of the incoming photon is labeled by $\mathbf{e}_0$ and its frequency by ω_0. The incoming photon is scattered to an outgoing photon of polarization $\mathbf{e}_S$ and frequency ω_0-ω_m, while a phonon of frequency ω_m is created.

In centimeter-gram-second (cgs) units, the differential scattering efficiency is given by

$$\frac{dS^m}{d\Omega} = |\mathbf{e}_S \cdot R^m \cdot \mathbf{e}_0|^2 = \frac{(\omega_0 - \omega_m)^4}{c^4} |\mathbf{e}_S \cdot \alpha^m \cdot \mathbf{e}_0|^2 \frac{\hbar}{2\omega_m}(n_m + 1). \quad (1)$$

In this equation, c represents the speed of light in vacuum. The phonon occupation numbers n_m are given by the Bose-Einstein distribution

$$n_m = \frac{1}{\exp(\hbar\omega_m / k_B T) - 1}. \quad (2)$$

The Raman susceptibility tensor $\alpha_\mathbf{m}$ is calculated within the density functional theory according to

$$\alpha^m_{ij} = \sqrt{\Omega_0} \sum_{\kappa,\beta} \frac{\partial \chi^{(1)}_{ij}}{\partial \tau_{\kappa\beta}} u_m(\kappa\beta), \quad (3)$$

where $\chi^{(1)}_{ij}$ is the electronic linear dielectric susceptibility tensor, which is related to the frequency-dependent dielectric permittivity by $\varepsilon^{(1)}_{ij} = 1 + 4\pi\chi^{(1)}_{ij}$. The latter is calculated in independent particle approximation [28]. Ω is the angle of collection in which the outgoing photon is scattered. The zone center phonon frequencies ω_m as well as the eigendisplacements $u_m(\kappa\beta)$ are calculated within the frozen phonon method. $\tau_{\kappa\beta}$ represents the displacement of atom κ in direction β.

A phonon mode is called *longitudinal* or *transversal* when the polarization vectors are parallel or perpendicular to the phonon wave vector $\mathbf{k}$, respectively. Longitudinal modes in polar materials couple to the long-ranging electric fields generated by the atomic displacement, which can be accounted for, e.g., by linear response methods. However, the intensity of scattering on the transversal phonon modes, the assignment of which is controversial and which we focus on in this work, is immediately obtained from the equations above.

B. Computational parameters

We have performed DFT calculations within the generalized gradient approximation [29] (GGA) in its PW91 formulation [30] as implemented in the VIENNA AB INITIO SIMULATION PACKAGE (VASP) [31,32]. Projector augmented wave [33,34] (PAW) potentials with projectors up to $l = 3$ for Nb and Ta and $l = 2$ for Li and O as well as a plane wave cutoff of 400 eV have been used. Thereby numbers of 3, 11, 11, and 6 valence electrons are considered for Li, Nb, Ta, and O, respectively. The rhombohedral phases of $LiTaO_3$ and $LiNbO_3$ are modeled with 10 atoms and two formula units per primitive cell. The atomic positions are relaxed to minimize the equilibrium forces to less than 0.001 eV/Å. The resulting lattice parameters $a_R^{\mathrm{LN}} = 5.495$ Å, $\alpha^{\mathrm{LN}} = 55.867^\circ$ and $a_R^{\mathrm{LT}} = 5.478$ Å, $\alpha^{\mathrm{LT}} = 55.950^\circ$ are in very close agreement with the commonly accepted experimental values ($a_R^{\mathrm{LN}} = 5.494$ Å, $\alpha^{\mathrm{LN}} = 55.871^\circ$ and $a_R^{\mathrm{LT}} = 5.474$ Å, $\alpha^{\mathrm{LT}} = 56.167^\circ$). The deviations from the experimental value of the lattice constant a_R and angle α_R are for both materials smaller than 0.4%. Frozen-phonon calculations [27] without symmetry constraints have been performed to determine the zone center phonon frequencies and eigenvectors. Atomic displacements of 0.05 Å in the direction of each Cartesian coordinate are considered for the calculation of the Hessian matrix. The k-space integrations in the electronic structure calculations are performed using Γ-centered $6 \times 6 \times 6$ meshes [35]. This corresponds to 216 irreducible points in the first Brillouin zone, when symmetry is switched off for frozen-phonon calculations.

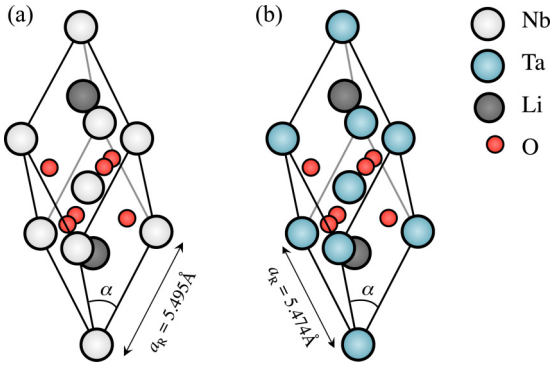

FIG. 1. (Color online) Rhombohedral primitive cells of (a) $LiNbO_3$ and (b) $LiTaO_3$ with their calculated rhombohedral lattice constants.

The frequency-dependent dielectric matrix $\varepsilon^{(1)}$ is calculated on the basis of the DFT wave functions and eigenenergies. Thereby 100 empty states were considered both for $LiTaO_3$ and $LiNbO_3$. This yields $\varepsilon^{(1)}$ values converged up to 1%. The Raman susceptibility tensor in Eq. (3) is calculated by finite differences, considering atomic displacements of 0.01 Å in the direction of each Cartesian coordinate. The calculated Raman intensities are renormalized with respect to the highest intensity. Thus, the relative peak intensity is the relevant parameter and not the absolute scattering efficiency, which is thus expressed in arbitrary units.

C. Raman modes in $LiTaO_3$ and $LiNbO_3$

Both ferroelectric lithium niobate and tantalate belong to the space group $R3c$ and have point group symmetry $3m$. The primitive cells contain two formula units each, corresponding to 10 atoms and therefore 30 vibrational degrees of freedom (see Fig. 1). In the framework of the group theory, vibrations with vanishing wave vector $\mathbf{k}$ can be divided—in first approximation—into $5A_1$, $5A_2$, and 10 (twofold degenerate) E phonon branches. One A and one E are the acoustic branches, while the remaining $4A_1$ and $9E$ optical branches can be measured both by Raman and infrared spectroscopy. The five A_2 fundamentals are Raman and infrared inactive. The A_1 modes are polarized along Z, while the doubly degenerate E modes are polarized in the X-Y plane.

The scattering geometry of the experiment performed in this work is described within the Porto notation $\mathbf{k}_0(\mathbf{e}_0,\mathbf{e}_S)\mathbf{k}_S$, where

TABLE I. Selection rules and Raman tensor elements for all investigated backscattering geometries. X,Y,Z refer to the orthogonal reference system for tensor properties. TO and LO label transverse and longitudinal optical modes, respectively.

Configuration	Symmetry	Eff. TO	Eff. LO
$\overline{X}(Y,Y)X$	A_1 TO, E TO	a^2+c^2	
$\overline{X}(Y,Z)X$	E TO	d^2	
$\overline{X}(Z,Y)X$	E TO	d^2	
$\overline{X}(Z,Z)X$	A_1 TO	b^2	
$\overline{Y}(X,X)Y$	A_1 TO, E LO	a^2	c^2
$\overline{Y}(X,Z)Y$	E TO	d^2	
$\overline{Y}(Z,X)Y$	E TO	d^2	
$\overline{Y}(Z,Z)Y$	A_1 TO	b^2	
$\overline{Z}(X,X)Z$	A_1 LO, E TO	c^2	a^2
$\overline{Z}(X,Y)Z$	E TO	c^2	
$\overline{Z}(X,Y)Z$	E TO	c^2	
$\overline{Z}(Y,Y)Z$	A_1 LO, E TO	c^2	a^2

$\mathbf{k}_0,\mathbf{k}_S$ are the propagation directions of incoming and scattered photons and $\mathbf{e}_0,\mathbf{e}_S$ are their polarization. The Porto notation refers to the orthogonal coordinate system XYZ commonly used for tensor properties. Thereby Z is parallel to the crystal c axis, X corresponds to one of the equivalent axis of the hexagonal structure and is therefore perpendicular to a mirror symmetry plane, and Y is chosen such that the system is right handed. Within the orthogonal coordinate system, the matrices for the components of the Raman tensor for the irreducible representations of the $3m$ point group are [36]

$$A_1(z)=\begin{pmatrix} a & 0 & 0\\ 0 & a & 0\\ 0 & 0 & b\end{pmatrix}, \tag{4}$$

$$E(y)=\begin{pmatrix} c & 0 & 0\\ 0 & -c & d\\ 0 & d & 0\end{pmatrix}, \tag{5}$$

$$E(-x)=\begin{pmatrix} 0 & -c & -d\\ -c & 0 & 0\\ -d & 0 & 0\end{pmatrix}. \tag{6}$$

The Raman tensor describes the contribution to the scattering intensity depending on the polarization direction of the incoming and scattered light, i.e., the selection rules. Depending on the scattering geometry A_1 or E modes as well as longitudinal or transversal modes can be observed. The A_1 tensor describes the scattering process in which the polarization of the incoming and scattered photons are parallel, while the E tensor describes the case in which the polarization of incoming and scattered photons is perpendicular. The modes observed for a given scattering geometry are compiled in Table I.

III. EXPERIMENT

The experiments have been carried out on a μ-Raman setup at room temperature in back-scattering geometry as described in Refs. [16,17]. The excitation source was provided by a frequency-doubled 532-nm Nd:YAG laser with 50 mW output power, while the spectral analysis was carried out on a spectrometer with an integrated Notch filter and holographic grating (KOSI Holospec $f/1.8$i) with an attached Andor Newton Charge-coupled Device (CCD) camera and an overall spectral resolution of about 2.5 cm^{-1}. Additionally, polarizers have been added in the excitation and detection path, which allows for defined scattering geometries. In contrast to previous work, no confocal pinhole was applied [16,17]. The neglect of a depth-resolved analysis ensures a large scattering and detection volume. Hence, nearly exclusively bulk phonons, which are the focus of this investigation, will contribute to the spectra. The importance of measuring stoichiometric samples has been outlined by Ridah *et al.*, as in congruent specimens broader and less resolved Raman bands appear [18]. Furthermore, defect bands could lead to a misleading mode assignment. The studied samples were both commercially available stoichiometric $LiTaO_3$ (DÖRER Elektrooptik GmbH and partner Deltronic Crystal Inc.) and stoichiometric $LiNbO_3$ (Roditi International Corporation), with lattice parameters as indicated in Sec. II B. The samples have been polished on the X, Y and Z faces for a smooth surface. Congruent lithium niobate and lithium tantalate are not object of this investigation.

In the experiment, Raman spectra have been obtained in the range from 100 to 1000 cm^{-1} in the scattering geometries summarized in Table I. There is neither experimental nor theoretical evidence of $LiNbO_3$- or $LiTaO_3$-related phonon modes at lower or higher frequencies. The main goal of this work is the identification and assignment of the zone center TO phonon modes. Therefore, not only the knowledge of the phonon frequencies at Γ but also the relative intensities in each spectrum are necessary. The spectral signatures of all detected phonons have been fitted with Lorentzian functions to obtain peak intensities (peak areas), FWHM, and peak frequencies. Following the usual procedure, the spectra have been recalculated based on the obtained values. This method is illustrated in Fig. 2 using the $LiNbO_3$ spectra recorded within the $\overline{X}(Y,Y)X$ geometry between 100 and 500 cm^{-1} as an example. The raw data (black curve) are best fitted by the 10 Lorentzian functions shown in light blue (gray). The sum of the single functions is the fitted spectrum, shown in the picture as a blue (gray) curve. The minor peak indicated at 194 cm^{-1} is a spectral feature which cannot be assigned to any first order scattering process (see, e.g., Ref. [26] and the discussion in the next section) and does not appear in the calculated spectra. Removing the corresponding Lorentzian from the spectrum yields the corrected spectrum shown in the picture as a dark blue (gray) curve, which can be readily compared with the DFT calculations. With this procedure the spectra are corrected for those peaks that could be assigned without ambiguity to multiphonon processes. Also, LO phonons were removed from the spectra for a direct comparison with the calculated values. If peaks did show a unresolvable overlap, both peaks have been fitted with a single Lorentzian. This was the case for the E TO_5 and E TO_6 in all geometries or the E TO_8 and A_1 TO_4 in $LiTaO_3$ in the $\overline{Y}(X,X)Y$ geometry. The measured spectra are renormalized with respect to the highest peak, so that the intensity of the following spectra are expressed in arbitrary units. The relative peak intensity and not the absolute value is thus relevant.

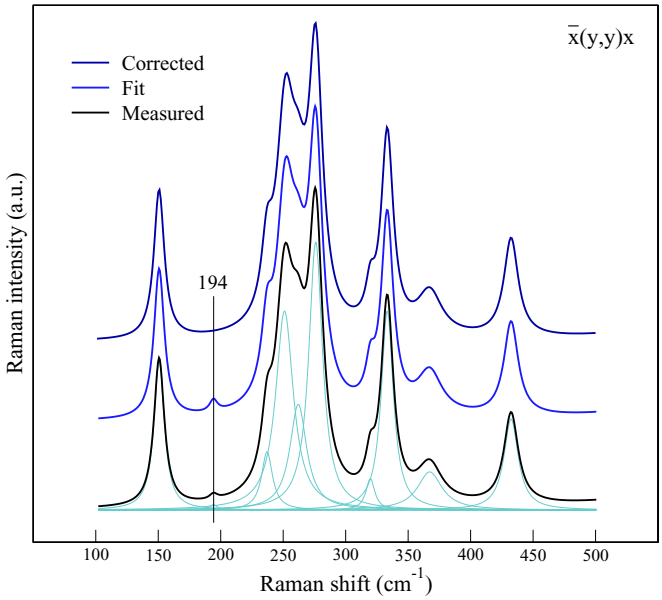

FIG. 2. (Color online) $LiNbO_3$ Raman spectra measured within the $\overline{X}(Y,Y)X$ geometry between 100 and 500 cm^{-1}. The raw data (black curve) are fitted by Lorentzian functions (in light blue [gray]), whose sum yields the fitted spectrum (blue [gray] curve). The latter can be corrected for spectral signatures that cannot be assigned to any first order process (dark blue [gray] curve). The raman intensity is expressed in arbitrary units.

IV. RESULTS

As $LiTaO_3$ and $LiNbO_3$ are very similar in many aspects, we employ the same procedure to investigate the two materials. The first step is the assignment of the A_1 TO modes. Relying on the selection rules shown in Table I, most modes can be assigned without uncertainty. The A_1 TO modes can be relatively easily identified within the $\overline{X}(Z,Z)X$ scattering configuration, as they are the only active modes in this geometry. The E TO modes can be detected with the $\overline{Z}(Y,X)Z$ setup instead. Unfortunately, only 8 of 9 modes can be detected in our experiment. The resulting data are shown in Tables II and III. From the comparison with other scattering geometries, e.g., $\overline{Z}(X,X)Z$, the A_1 longitudinal modes can be identified. For both $LiTaO_3$ and $LiNbO_3$ the experimentally detected LO and TO A_1 modes are in good agreement with the literature [18–20,37–41] and shall not be further discussed at this point.

For the assignment of the E modes, a comparison between calculated and measured Raman intensity is indeed necessary. In this respect, a word of caution is in order. While the measured peak width provides information, e.g., about stoichiometry, the peak form is chosen to be Lorentzian with a constant width of 12 cm^{-1} for all the calculated Raman spectra shown in the following [42].

This might introduce some deviation from the experiment whereas broad peaks overlap with minor peaks, resulting in an increased apparent intensity of the minor peak.

The dielectric permittivity is a symmetric tensor. Therefore no differences in the calculated spectra are observed by swapping the polarization of incoming and scattered photon: $(X,Y) = (Y,X)$. Furthermore, the propagation direction (wave vector) of the incoming and scattered vectors do not enter in the calculation. All the spectra are calculated for an incoming photon frequency of 532 nm, which corresponds to the energy of the laser employed in the experiment.

Since the longitudinal modes are not considered within our computational approach, the measured Raman peaks assigned to the longitudinal modes are removed from the spectra during the fitting procedure described in Sec. III. This only affects the E modes appearing in the $\overline{Y}(X,X)Y$ configuration and the A_1 modes according to Table I. This procedure does not introduce any uncertainty in our approach, as all appearing longitudinal modes can be unambiguously identified.

TABLE II. Calculated and measured frequencies of the Raman active phonon modes in $LiNbO_3$. E TO_5 and E TO_6 have similar frequencies and cannot be resolved within Raman spectroscopy. All frequencies are in cm^{-1}.

Symmetry	Mode	Theory	Exp.	Mode	Exp.
A_1	TO_1	239	252–255	LO_1	274
A_1	TO_2	289	275–276	LO_2	330
A_1	TO_3	353	333–334	LO_3	422
A_1	TO_4	610	633	LO_4	871
E	TO_1	148	150–151	LO_1	192
E	TO_2	216	237	LO_2	237
E	TO_3	262	262–263	LO_3	297
E	TO_4	323	320–321	LO_4	–
E	TO_5	380	367–369	LO_5	369
E	TO_6	391	367–369	LO_6	428
E	TO_7	423	432	LO_7	456
E	TO_8	579	580–581	LO_8	–
E	TO_9	667	664	LO_9	877

A. $LiNbO_3$

Table II shows the measured and calculated frequencies of the optical transverse and longitudinal modes in $LiNbO_3$. The measured values are given within a small range due to minor

TABLE III. Calculated and measured frequencies of the Raman active phonon modes in $LiTaO_3$. E TO_5 and E TO_6 have similar frequencies and cannot be resolved within Raman spectroscopy. All frequencies are in cm^{-1}.

Symmetry	Mode	Theory	Exp.	Mode	Exp.
A_1	TO_1	209	209–210	LO_1	255
A_1	TO_2	286	256–257	LO_2	355
A_1	TO_3	376	359–360	LO_3	403
A_1	TO_4	591	600	LO_4	866
E	TO_1	144	143	LO_1	190
E	TO_2	199	210	LO_2	
E	TO_3	253	254–257	LO_3	279
E	TO_4	319	315–317	LO_4	
E	TO_5	409	383–384	LO_5	381
E	TO_6	420	383–384	LO_6	453
E	TO_7	459	460–465	LO_7	
E	TO_8	590	592	LO_8	660
E	TO_9	669	661–662	LO_9	866

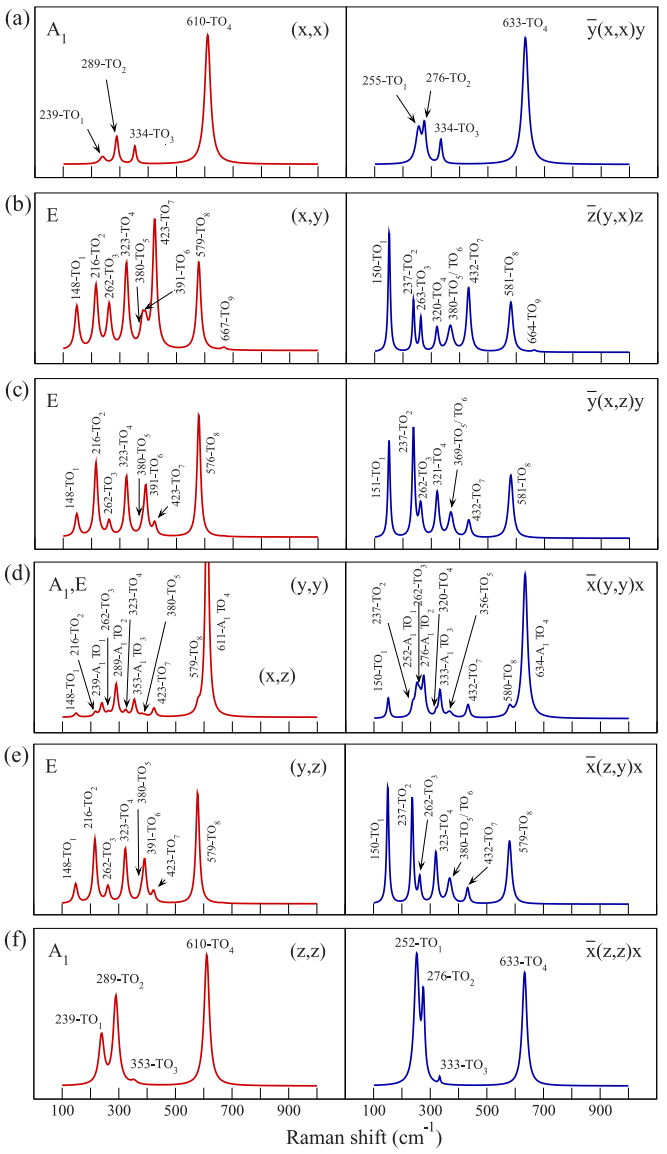

FIG. 3. (Color online) Calculated (left-hand side) and measured (right-hand side) $LiNbO_3$ Raman spectra for all different scattering geometries. The Raman intensity is expressed in arbitrary units.

differences observed for different scattering geometries. The calculated modes show a mean deviation of 10.7 cm^{-1} from the measured values and can be considered in good agreement with the experiment. The largest deviation occurs for the A_1 TO_4 and amounts to 23 cm^{-1}. Both calculated and measured values are also in agreement with the results available in the literature [18,20].

The Raman spectra of $LiNbO_3$ measured and calculated for all different scattering configurations are compared in Fig. 3. Within $\overline{X}(Z,Z)X$ [Fig. 3(f)], both the incoming and scattered photons are polarized along the Z direction. Thus, only A_1 TO modes have a nonvanishing scattering efficiency in this configuration. All four TO modes are correctly predicted from the theory, both in position and intensity. We observe that while TO_1, TO_2, and TO_4 have similar, strong Raman intensity, TO_3 appears both in the measured and calculated spectra as a very small-sized peak. This can be readily understood on the basis

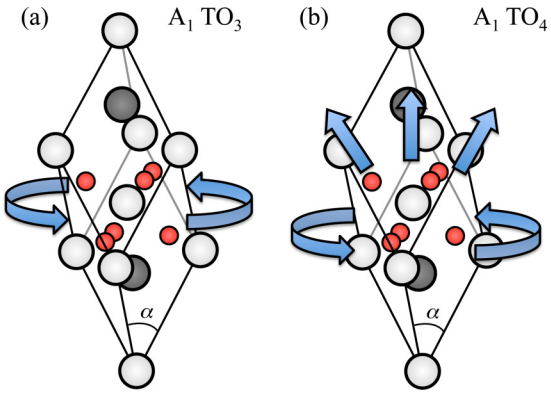

FIG. 4. (Color online) Eigenvectors of the A_1 vibrational transversal branches TO_3 and TO_4 of $LiTaO_3$ and $LiNbO_3$. Both modes only concern displacements of the oxygen sublattice. Arrows schematically represent the displacement patterns.

of the mode eigenvector. A_1 TO_3 is a rigid rotation of the oxygen octahedra around the crystal c axis [see Fig. 4(a)]. The atomic displacement preserves the crystal symmetry and does not modify the cation-anion distances. It thus results in a minor modification of the crystal polarization and therefore in strongly reduced Raman intensity. While the strong intensity difference between the A_1 TO_1, TO_2, and the A_1 TO_3 bands is correctly reproduced in our calculations, TO_2 appears in the calculation slightly stronger than TO_1, in contrast to the measurements. However, this does not mean that the two bands are inverted in our theoretical model, as the comparison of the phonon eigenvectors with the descriptions available in the literature readily confirms the assignment in Fig. 3(f). Moreover, the relative intensity of A_1 TO_1 and TO_2 is correctly predicted for the (X,Z) and (Y,Y) scattering geometries. A detailed description of the phonon eigenvectors of the A_1 TO modes can be found in our previous work [43].

The A_1 modes can be also detected with the $\overline{Y}(X,X)Y$ [Fig. 3(a)] configuration. Within this geometry the dominant peak is the TO_4. This mode consists of a rotation of the oxygen octahedra around the crystal c axis combined with an expansion of the cage itself [see Fig. 4(b)]. Having both displacement in the X-Y plane as well as along Z, the mode can be efficiently excited in the $\overline{X}(Z,Z)X$, $\overline{Y}(X,X)Y$, and in the $\overline{X}(Y,Y)X$ [Fig. 3(d)] configuration as well.

The E modes can be also observed with the remaining configurations $\overline{Z}(X,Y)Z$, $\overline{X}(Z,Y)X$, and $\overline{Z}(X,Z)Z$.

The latter scattering geometry allows for the simultaneous detection of the E modes. Unfortunately, none of the configurations allows for the detection of all 9 E TO modes, as only 7 or 8 peaks appear in the spectra. For this reason many contradictory assignments can be found in the literature, which is therefore no real help in the mode assignment. In particular, several inconsistent assignment of the two "missing" modes have been proposed. The oldest assignment date back to the works of Kaminow [37] and Barker [38] (both 1967). The first proposed modes at 92 and 630 cm^{-1} and the second at 180 and 610 cm^{-1}, which were interpreted as mixed modes, though. Claus [39] (1972) reported modes at 668 and 743 cm^{-1}. Yang and coworkers [40] (1987) interpreted the modes at 670 and 743 cm^{-1} as combination bands, suggesting the presence of

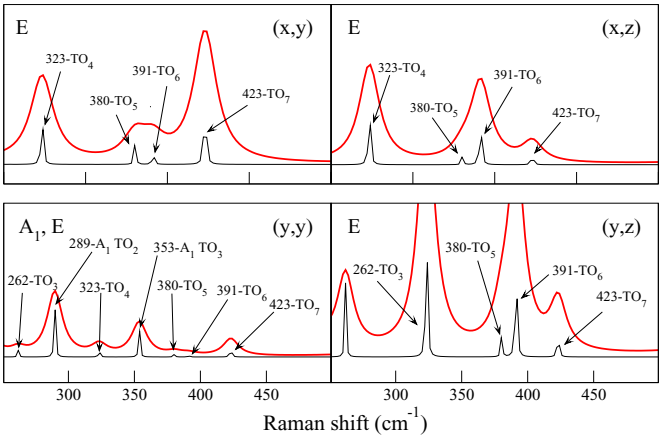

FIG. 5. (Color online) Enlargement of the calculated $LiNbO_3$ Raman spectra of Fig. 3 for all scattering configurations allowing the detection of the E-TO modes. The red (gray) line corresponds to the spectra shown in Fig. 3, and the black curve shows the exact position of the Raman peaks. The Raman intensity is expressed in arbitrary units.

modes at 152 and 530 cm^{-1}. Ridah [18] and Repelin [41] (1997 and 1999) agree about the presence of regular modes at 180 and 610 cm^{-1}, which were previously interpreted by Barker as mixed modes. More recently, Margueron [26] (2012) suggested that the E TO_5 and TO_6 have close frequencies and that TO_6 has vanishing oscillator strength. From the theoretical point of view, the two missing modes were predicted by Parlinski [19] and Caciuc [20] (both 2000) at 423 and 690 cm^{-1}, and at 167 and 617 cm^{-1}, respectively. Hermet [25] (2007) suggested that the TO_5 and TO_6 modes are not the same experimental Raman mode but are two different E TO modes, the first mode only being visible by infrared spectroscopy and the second only being visible by Raman spectroscopy.

Our assignment of the E modes can be best understood from the spectra recorded with the $\overline{Z}(X,Y)Z$ [Fig. 3(b)] configuration. In this configuration 8 modes can be easily assigned to the calculated eigenvectors, the only uncertainty regarding TO_5 and TO_6. A comparison with the calculated spectra reveals that the TO_5 und TO_6 are two distinct modes that always appear in Raman as a single peak, due to their closeness in energy (calculated $\Delta\nu$ value 9 cm^{-1}) and relatively broad peaks. This is in agreement with the assignment previously proposed by Hermet [25]. However, depending on the scattering configuration, the TO_5 might have higher Raman intensity than the TO_6. The TO_6 has higher Raman intensity within the (X,Z) and (Y,Z) scattering geometry, while TO_5 is stronger in (X,Y) (see Fig. 5). In the (Y,Y) scattering geometry both modes have vanishing intensity. The theoretical predictions are corroborated by the Raman measurements. Indeed, while it is not possible to discriminate between the peaks in the experiment, which are fitted by a single Lorentzian, the fit is centered at 367 cm^{-1} within the (X,Y) and (Y,Y) scattering configurations, while it is shifted to somewhat higher frequencies (i.e., centered at 369 cm^{-1}) within the (X,Z) and (Y,Z) scattering configurations. This suggests that in the first case the TO_5 mode has a higher intensity than the TO_6, while in the second case TO_6 becomes dominant, as predicted from the theory. Our assignment of the E modes thus confirms the most recent assignment proposed by Hermet [25] and Margueron [26].

The $\overline{Z}(Y,X)Z$ configuration is furthermore particularly interesting, as it is the only configuration that allows for the detection of the E TO_9. E TO_9 has a small scattering efficiency both in the calculated and measured spectra and can only be observed with very low intensity. However, the comparison of the calculated spectra with the records of the $\overline{Z}(Y,X)Z$ backscattering configuration shows that the peak at 664 cm^{-1} is a regular Raman mode and not a second-order process.

Summarizing, as in the case of the A_1 modes, also in the case of the E modes the overall agreement between theory and experiment is noticeably good, both concerning peak position and intensity. As a general feature, the intensity of the calculated low-frequency peaks slightly underestimates the experimental value.

B. $LiTaO_3$

Table III shows the measured and calculated frequencies of the optical transverse modes in $LiTaO_3$. With a mean deviation of 10.8 cm^{-1} from the measured values, the calculated frequencies have accuracy similar to that in the case of $LiNbO_3$. The agreement of measured and calculated phonon energies can be considered satisfactory. Available data from the literature [26,40,41,44–47], are in agreement with both the measured and calculated frequencies.

In analogy with $LiNbO_3$ the comparison of the measured and calculated spectra in the scattering configurations $\overline{Z}(Y,Y)Z$ [Fig. 6(f)] and $\overline{Z}(X,Y)Z$ [Fig. 6(b)] yields the assignment of all transversal modes of A_1 and E symmetry, respectively. Exactly as in the case of $LiNbO_3$, the TO_5 and TO_6 bands appear in the experiment as a single broad peak. Their frequency is indeed very close (calculated value $\Delta\nu = 11\,cm^{-1}$). Depending on the scattering configuration either TO_5 or TO_6 outweighs the other mode, resulting in a single detectable band.

The calculated intensity of the Raman spectra for all investigated polarization directions is in very good agreement with the measured values, apart from the underestimation of the intensity of the experimental peak assigned to the A_1 TO_4 + E TO_8 in the $\overline{X}(Y,Y)X$ [Fig. 6(d)]. This is due to the fact that the intensity of the two modes sums up in the experiment, while this is not the case for the calculated spectra.

The Raman spectra of $LiTaO_3$ and $LiNbO_3$ are overall rather similar, with one single but relevant difference: the E TO_9 band. The Raman behavior of this mode in the two oxides is strikingly different, as the mode is hardly detectable in $LiNbO_3$, while it is one of the strongest modes in $LiTaO_3$. While pronounced differences are expected for modes involving Ta and Nb, respectively, it is surprising to observe large differences in modes that only involve the oxygen sublattice. Indeed, the eigenvector of this mode represents a distortion of the oxygen cage, precisely the elongation along one of the three equivalent XZ planes (see Fig. 7). The E TO_9 mode is thus a pure oxygen mode and its frequencies in $LiTaO_3$ and $LiNbO_3$ are therefore very similar. As the phonon eigenvectors in the two materials are nearly identical, the reasons for the mode quenching in $LiNbO_3$ have to be searched

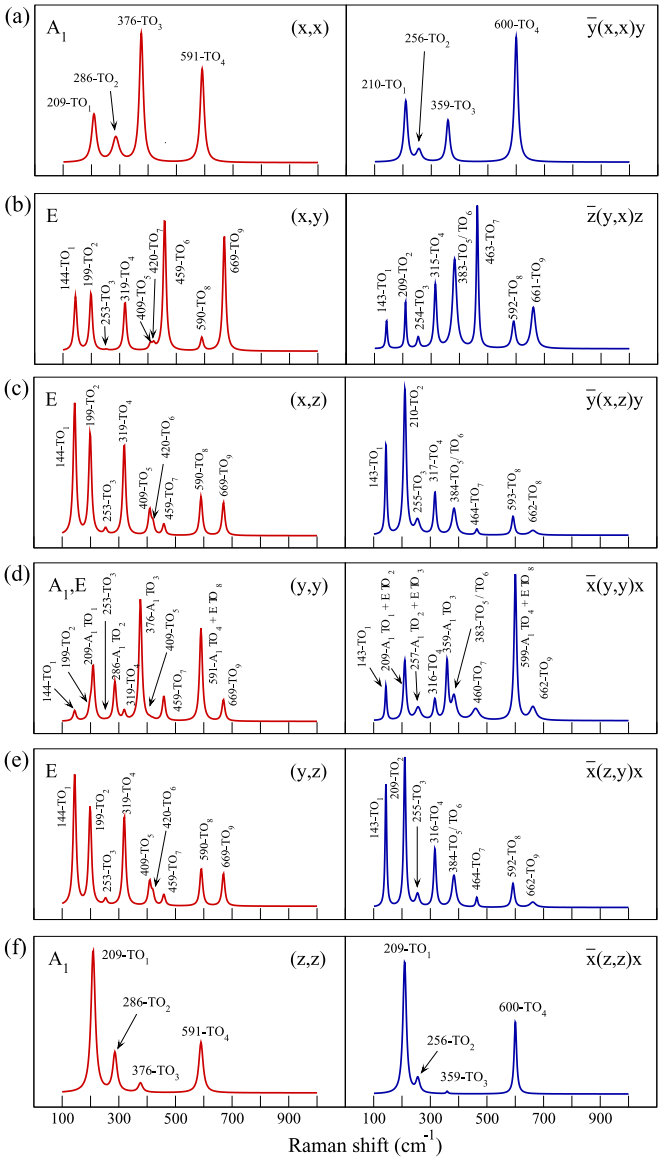

FIG. 6. (Color online) Calculated (left-hand side) and measured (right-hand side) $LiTaO_3$ Raman spectra for all different scattering geometries. The Raman intensity is expressed in arbitrary units.

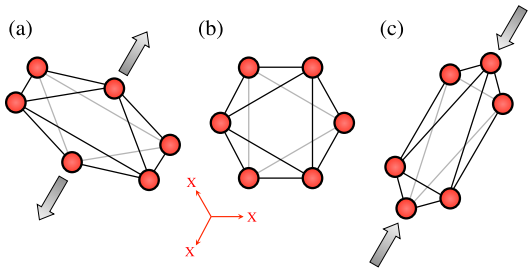

FIG. 7. (Color online) Eigenvectors of the E vibrational transversal branch TO_9 of $LiTaO_3$ and $LiNbO_3$. The undistorted oxygen octahedron (b) is stretched along the XZ plane [(a), (d)]. In both materials the mode only concerns displacements of the oxygen sublattice. Arrows represent the distortion direction.

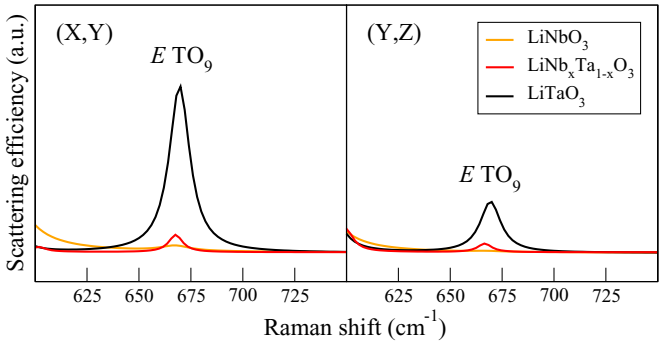

FIG. 8. (Color online) Calculated Raman intensity of the $LiNb_xTa_{1-x}O_3$ mixed crystals with $x = 0$, 0.5, and 1 for the (X,Y) and (Y,Z) tensor components.

for in the polarizability differences of the respective bonds involved in the two crystals. One possible explanation might be given by the different Nb-O and Ta-O bond lengths and strengths in the two systems. As Nb and Ta have exactly identic ionic radii [48], the average calculated Nb-O bond length in $LiNbO_3$ of 2.02 Å corresponds to a weaker Nb-O bond than the average Ta-O bond with a calculated length of 1.99 Å in $LiTaO_3$. Thus, the TO_9 phonon distortion results in a larger relative deformation of the Ta-O bond in $LiTaO_3$ than of the Nb-O bond in $LiNbO_3$, with corresponding larger modification of the polarizability. This possible explanation is in agreement with the fact that also the other phonon bands involving solely a displacement of the oxygen ions (e.g., A_1 TO_3 and TO_4) have a stronger relative intensity in $LiTaO_3$ than in $LiNbO_3$. In order to verify our assumption, we have calculated the Raman intensity for ordered $LiNb_xTa_{1-x}O_3$ mixed crystals with $x = 0.5$. Modeling mixed crystals as ordered alloys is certainly an approximation, which, however, suffices for our test purposes. The average Nb,Ta-O distance in these crystals amounts to 2.00 Å and is thus in between the two end compounds. The results of our calculation are shown in Fig. 8 for the Raman tensor components (X,Y) and (Y,Z). As expected, the calculated intensity of the E TO_9 mode for the mixed crystals is between the mode intensity in $LiTaO_3$ and in $LiNbO_3$. In further agreement with Ref. [26], we find the Raman intensity of the E TO_9 mode in $LiNb_xTa_{1-x}O_3$ mixed crystals to be a sublinear function of the Ta concentration.

V. CONCLUSIONS

The vibrational properties of bulk $LiTaO_3$ and $LiNbO_3$ were addressed here by combining nonresonant μ-Raman spectroscopy with scattering efficiency calculations within density-functional theory for all possible scattering geometries. A generally very good agreement between measured and calculated peak positions and intensities has been achieved that allowed for a conclusive assignment of the TO phonon modes. In particular, all A_1 and E transversal optical modes, which have been controversially discussed for many decades, could be unambiguously identified.

Furthermore, the intensity of the measured Raman peaks could be understood on the basis of the atomic displacement of the corresponding phonon mode. In particular, it is shown

that the TO_5 and TO_6 are very close in energy and appear as a single Raman peak both in $LiTaO_3$ and $LiNbO_3$. Depending on the scattering geometry, either TO_5 or TO_6 can be detected; however, depending on the particular configuration, one mode dominates over the other, resulting in a single Raman band. This shows the importance of an approach capable of reliable prediction of the Raman scattering efficiency for a given configuration setup. Indeed, Raman scattering efficiencies for piezoelectric crystals and their angular variations are dependent upon whether electrostatic forces predominate over anisotropy in the short-range interatomic forces or vice versa and are thus hard to predict.

The E TO_9 mode has a different behavior in $LiTaO_3$ and $LiNbO_3$. While it is only detectable with a very low intensity in the $\overline{Z}(Y,X)Z$ scattering geometry in $LiNbO_3$, it appears as a strong Raman peak in several configurations in $LiTaO_3$. The difference is tentatively explained by the larger relative distortion of the Ta-O bond in $LiTaO_3$ than of the Nb-O bond in $LiNbO_3$.

The combination of theoretical and experimental Raman spectroscopy employed here to clarify the assignment of bulk phonon modes is expected to be very helpful to investigate the Raman intensity modulation at extended defects or domain walls in ferroelectric materials [16].

ACKNOWLEDGMENTS

The Deutsche Forschungsgemeinschaft (DFG) is acknowledged for the financial support by the Sonderforschungsbereich TRR 142 and FOR1700. All the calculations were performed at the Paderborn Center for Parallel Computing (PC^2) and at High Performance Computing Center in Stuttgart (HLRS).

[1] R. S. Weis and T. K. Gaylord, Appl. Phys. A: Solids Surf. **37**, 191 (1985).
[2] G. G. Bentini, M. Bianconi, M. Chiarini, L. Correra, C. Sada, P. Mazzoldi, N. Argiolas, M. Bazzan, and R. Guzzi, J. Appl. Phys. **92**, 6477 (2002).
[3] K. Buse, A. Adibi, and D. Psaltis, Nature (London) **393**, 665 (1998).
[4] T.-C. Lee, J.-T. Lee, M. A. Robert, S. Wang, and T. A. Rabson, Appl. Phys. Lett. **82**, 191 (2003).
[5] F. Agullo-Lopez *et al.*, *Properties of Lithium Niobate*, EMIS data reviews series (INSPEC/Institute of Electrical Engineers, London, 2002).
[6] T. Volk and M. Wöhlecke, *Lithium Niobate: Defects, Photorefraction, and Ferroelectric Switching*, edited by R. Hull, J. Parisi, R. M. Osgood Jr., and W. H, Springer Series in Material Science Vol. 115 (Springer-Verlag, Berlin, 2008).
[7] D. J. Gardiner and P. R. Graves, eds., *Practical Raman Spectroscopy* (Springer-Verlag, Berlin, 1989).
[8] E. Buixaderas, I. Gregora, M. Savinov, J. Hlinka, L. Jin, D. Damjanovic, and B. Malic, Phys. Rev. B **91**, 014104 (2015).
[9] A. Bartasyte, S. Margueron, J. Kreisel, P. Bourson, O. Chaix-Pluchery, L. Rapenne-Homand, J. Santiso, C. Jimenez, A. Abrutis, F. Weiss, and M. D. Fontana, Phys. Rev. B **79**, 104104 (2009).
[10] R. Mouras, M. D. Fontana, P. Bourson, and A. V. Postnikov, J. Phys.: Condens. Matter **12**, 5053 (2000).
[11] R. Quispe-Siccha, E. V. Mejía-Uriarte, M. Villagrán-Muniz, D. Jaque, J. García Solé, F. Jaque, R. Y. Sato-Berrú, E. Camarillo, J. Hernández A., and H. Murrieta S., J. Phys.: Condens. Matter **21**, 145401 (2009).
[12] A. Ridah, M. D. Fontana, and P. Bourson, Phys. Rev. B **56**, 5967 (1997).
[13] K. Fleischer, S. Chandola, N. Esser, W. Richter, and J. F. McGilp, Phys. Rev. B **67**, 235318 (2003).
[14] P. S. Zelenovskiy, V. Y. Shur, P. Bourson, M. D. Fontana, D. K. Kuznetsov, and E. A. Mingaliev, Ferroelectrics **398**, 34 (2010).
[15] M. D. Fontana, R. Hammoum, P. Bourson, S. Margueron, and V. Y. Shur, Ferroelectrics **373**, 26 (2008).
[16] G. Berth, W. Hahn, V. Wiedemeier, A. Zrenner, S. Sanna, and W. G. Schmidt, Ferroelectrics **420**, 44 (2011).
[17] S. Sanna, G. Berth, W. Hahn, A. Widhalm, A. Zrenner, and W. G. Schmidt, Ferroelectrics **419**, 1 (2011).
[18] A. Ridah, P. Bourson, M. D. Fontana, and G. Malovichko, J. Phys.: Condens. Matter **9**, 9687 (1997).
[19] K. Parlinski, Z. Q. Li, and Y. Kawazoe, Phys. Rev. B **61**, 272 (2000).
[20] V. Caciuc, A. V. Postnikov, and G. Borstel, Phys. Rev. B **61**, 8806 (2000).
[21] M. Cardona and G. Güntherodt, eds., *Light Scattering in Solids III*, Topics in Applied Physics, Vol. 51 (Springer-Verlag, Berlin, 1982).
[22] H. Haken, *Quantenfeldtheorie des Festkörpers* (B.G. Teubner, Stuttgart, 1973).
[23] D. Rappoport, Ph.D. thesis, Karlsruher Institut für Technologie, 2007 (unpublished).
[24] M. Veithen, X. Gonze, and P. Ghosez, Phys. Rev. B **71**, 125107 (2005).
[25] P. Hermet, M. Veithen, and P. Ghosez, J. Phys.: Condens. Matter **19**, 456202 (2007).
[26] S. Margueron, A. Bartasyte, A. M. Glazer, E. Simon, J. Hlinka, I. Gregora, and J. Gleize, J. Appl. Phys. **111**, 104105 (2012).
[27] W. G. Schmidt, F. Bechstedt, and G. P. Srivastava, Phys. Rev. B **52**, 2001 (1995).
[28] M. Gajdoš, K. Hummer, G. Kresse, J. Furthmüller, and F. Bechstedt, Phys. Rev. B **73**, 045112 (2006).
[29] J. P. Perdew, J. A. Chevary, S. H. Vosko, K. A. Jackson, M. R. Pederson, D. J. Singh, and C. Fiolhais, Phys. Rev. B **46**, 6671 (1992).
[30] J. P. Perdew and Y. Wang, Phys. Rev. B **33**, 8800 (1986).
[31] G. Kresse and J. Furthmuller, Comput. Mater. Sci. **6**, 15 (1996).
[32] G. Kresse and J. Furthmuller, Phys. Rev. B **54**, 11169 (1996).
[33] P. E. Blöchl, Phys. Rev. B **50**, 17953 (1994).
[34] G. Kresse and D. Joubert, Phys. Rev. B **59**, 1758 (1999).
[35] H. J. Monkhorst and J. D. Pack, Phys. Rev. B **13**, 5188 (1976).
[36] R. F. Schaufele and M. J. Weber, Phys. Rev. **152**, 705 (1966).

[37] I. P. Kaminow and W. D. Johnston, Phys. Rev. **160**, 519 (1967).
[38] A. S. Barker and R. Loudon, Phys. Rev. **158**, 433 (1967).
[39] R. Claus, G. Borstel, E. Wiesendanger, and L. Steffan, Z. Naturforsch. **27**, 1187 (1972).
[40] X. Yang, G. Lan, B. Li, and H. Wang, Phys. Status Solidi B **142**, 287 (1987).
[41] Y. Repelin, E. Husson, F. Bennani, and C. Proust, J. Phys. Chem. Solids **60**, 819 (1999).
[42] This value has been chosen as the measured peaks have a width between 10 and 15 cm^{-1}.
[43] S. Sanna, A. Riefer, S. Neufeld, W. G. Schmidt, G. Berth, M. Rüsing, A. Widhalm, and A. Zrenner, Ferroelectrics **447**, 63 (2013).
[44] C. A. Gautier, M. Mérian, and J. Etchepare, J. Phys.: Condens. Matter **12**, 7175 (2000).
[45] R. E. Cohen, Ferroelectrics **153**, 37 (1994).
[46] C. Raptis, Phys. Rev. B **38**, 10007 (1988).
[47] V. Caciuc and A. V. Postnikov, Phys. Rev. B **64**, 224303 (2001).
[48] R. Shannon, Acta. Cryst. A **32**, 751 (1976).